3-D Full-Wave Electromagnetic Modeling for Breast Microwave Tomography

Elia A. Attardo*, Andrea Borsic†, Giuseppe Vecchi*, and Paul M. Meaney†
*Politecnico di Torino
Corso Duca Degli Abruzzi 24, Turin, 10129, Italy
Email: {elia.attardo, giuseppe.vecchi}@polito.it
†Thayer School Of Engineering
Dartmouth College, 8000 Cummings Hall, Hanover, NH 03755, USA
Email: {andrea.borsic, paul.m.meaney}@dartmouth.edu

***Abstract*—This paper presents a full-wave, whole-system modeling of Microwave Imaging Tomography (MWT) systems, to be used as forward model in reconstruction (inverse) algorithms. The full geometry including antennas and their ports is simulated via a Finite Element Method (FEM) approach. A new technique is used to compute the antenna operation in the system, which provides a general method to enforce the excitation as a specific modal distribution and to extract the voltage and current from the employed antenna. We report results for a complete Microwave Imaging (MWI) system with comparison between measured and simulated data.**

***Index Terms*—Breast cancer detection, microwave imaging, finite element methods, monopole antennas, admittance matrix.**

I. Introduction

Microwave Imaging (MWI) has recently developed into a promising technique for breast cancer detection. Electrical permittivity and conductivity are known to differ between benign and malignant breast tissues for a wide range of the microwave spectrum [1]. The ability to non-invasively map these properties is therefore desirable and constitutes a new way of detecting cancer. Unlike radar based techniques, which have been proposed in literature for piece-wise homogeneous domains [2], tomographic approaches are suitable for recovering the dielectric properties of a heterogeneous medium such as the breast. Microwave tomography (MWT) is based on the use of a number of antennas (e.g. 8 to 16), arranged on a circle which surrounds the breast. One antenna is used for emitting an electromagnetic (EM) wave, which propagates through the breast, and the other antennas measure the received field intensity and phase. The transmitting antenna number is incrementally changed to provide measurement data from all surrounding directions. This allows collection of a dataset which contains information about the distribution of electrical properties in the volume of the breast. Image reconstruction is based on an inverse problem formulation, where a forward model is fitted to the measurements. By acting on the distribution of electrical properties in the model it is possible to fit simulated measurements to real measurements, and to estimate the true distribution of electrical properties. The model fitting is formulated as a least squares problem, incorporating a Tikhonov regularization ([3]) since the inversion is ill-posed. Ill posedeness is caused by the fact that in MWT fast spatial distributions of conductivity and permittivity result in very small variations in the measured data. This makes the recovery of fine spatial details difficult since the relative features in the data can be confounded with errors and noise.

In order to optimize image quality it is necessary, therefore, to maximize instrumentation accuracy and reduce model errors as much as possible. This allows matching synthetic and measured data to the precision needed to distinguish small but important data features that carry information of the finer spatial details of the electrical property distribution.

In the present manuscript we discuss the development and implementation of a novel forward model for MWT based on the Edge Finite Element Method (Edge FEM). For its first implementation we apply this model to a breast microwave imaging system developed at Dartmouth College [4]. Although the proposed modeling approach is general, it can be used for other MWT systems. The forward problem is formulated with a 3D curl-curl Helmholtz equation using zero order Whitney forms [5] as edge elements. This formulation is generally superior to traditional FEM formulations where field variables are associated to nodes ([6]). Edge FEM also compares favorably to Finite Difference Time Domain (FTDT) methods in terms of accuracy since FEM elements can be small near antennas, where the electric field varies rapidly and where small elements allow more accurate description of the antenna geometry. Larger elements can be used in regions far from the antennas, where the electric field varies more slowly. We regard this as an important step forward in achieving improved image quality and resolution in MWT compared to previous FDTD or nodal FEM based ([6]). In the present manuscript we derive variational methods, similar to [7], [8], and for describing antenna ports, associated excitations and received signals, and discuss and implement optimal conditions at the boundary of the imaging volume. Alternatively to the approach proposed in [9], (which has been addressed as the most complete work in modeling a tomographic MWI system by [10]), we provide a more general formulation in the following sections.

The manuscript is organized as follows: Section II describes the design and hardware architecture of the MWT system. Section III describes the model of the system and specific details of Edge FEM implementation, methods for describing

the excitations and received fields at the antennae ports, and absorbing boundary conditions. In Section IV we present experimental results, where several test cases are used to compare real measurements from the MWT system to synthetic values from the model. Finally, Section V summarizes this presentation.

II. Microwave breast tomography system

In this section we describe the principal characteristics of the MWT system. The breast imaging system [4] comprises 16 monopole antennas which are mounted circularly inside a cylindrical Plexiglas tank, which is open at the top as illustrated in Fig. 1(a). The function of the tank is to hold a water/glycerin bath that presents a good impedance match at the interface with the breast surface, minimizing reflections of the propagating fields as they enter the body. The bath, which has a conductivity of 0.5 to 2.0 S/m over the operating frequency range (see Fig. 7 for more details on the bath electrical properties), performs the function of sufficiently attenuating the fields to eliminate the possibility of unwanted multi-path signals. While the loss through the medium is high, heterodyne receivers can measure signals down to -135 dBm which is sufficient given the short propagation paths.

Figure 1(b) shows a view of the entire system, where the tank and antennas are visible on the right part of the photograph, and the electronics on the left. The diameter of the tank is 28 cm and the height is 20 cm. Fig. 1(c) shows the system with the bed on top. The patient lays prone on top of the system, which is soft, and inserts her breast in the opening. The breast will therefore be pendant beneath the level of the table, and inside the circle of antennas.

The monopole antennas employed in the system have a simple, omnidirectional design, and are formed by a rigid 50 Ω coaxial cable, 3.58 mm diameter, where the metallic shield has been stripped for the last 3.4 cm from the top, effectively allowing the core conductor to radiate, (Fig. 2). This antenna exhibits a wideband behavior when fully immersed in the lossy bath [11] (from 500 MHz up to 3000 MHz), and results in an almost spherical radiation pattern which emanates from the stripped part (see Fig. 9).

Fig. 2. Monopole antenna: coaxial cable with the outer metal conductor stripped from the termination. The region free from the shield acts as an active zone (transmitting zone), as it couples with the surrounding medium.

The system operates over the frequency range of 500 to 3000 MHz, and the electronics are custom designed components and can detect signals down to -135 dBm. The transmitted power for imaging is 5 mW or less.

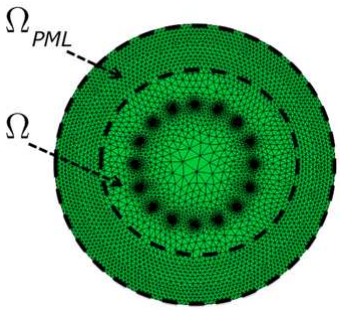

Fig. 3. Meshed domain, cross-section: Ω_{PML} is the region occupied by PML; region Ω is the imaging domain; the fields emitted by the antennas propagate through this region.

III. System Modeling

The microwave tomography system can be described by and N-port model, each port representing an antenna port, as illustrated in Fig. 4. The system is operated by applying an excitation to one port and by measuring responses at the remaining ports. The measurements depend on the propagation and scattering phenomena that occur inside the volume of the tank, and are used to reconstruct the spatial distribution of electrical conductivity and permittivity within the breast. A single measurement consists of the sensing voltage V_j, received at the jth antenna port, when a single frequency excitation of V_i is applied to the ith port. The objective of this treatment is to develop a model that links the MWT measurements to the spatial distribution of electrical properties inside the tank's volume, so that through an inverse procedure it might be possible to estimate them. For the purpose of modeling we divide the cylindrical volume of the tank into two concentric regions as illustrated in Fig. 3.

The inner region, region Ω, is the actual discretized volume inside the tank. This region is filled with the water/glycerin bath, and includes the antenna array where the breast is present during examinations, and where electrical properties are estimated. The second region, (region $\Omega_{PML} = \cup_{i=1}^{3}\Omega_i$ in Fig. 6), extends radially from the end of region Ω, to the walls of the tank. This region is used for modeling the progressive attenuation of the fields, which for any practical purpose are completely attenuated by the lossy bath before reaching the tank walls. As discussed in Sec. III-B4, a Perfectly Matched Layer will be implemented in this region, absorbing the fields that propagate in it.

A. Numerical Formulation by the Edge Finite Element Method

For a single frequency excitation, the propagation and scattering of electromagnetic waves inside the volume of the MWT tank is described by the Maxwell's equations. Disregarding the source terms for the moment:

$$\nabla \times \mathbf{E} = -j\omega \underline{\underline{\mu}} \cdot \mathbf{H} \tag{1}$$

$$\nabla \times \mathbf{H} = j\omega \underline{\underline{\epsilon}} \cdot \mathbf{E} \tag{2}$$

$$\nabla \cdot (\underline{\underline{\epsilon}} \cdot \mathbf{E}) = 0 \tag{3}$$

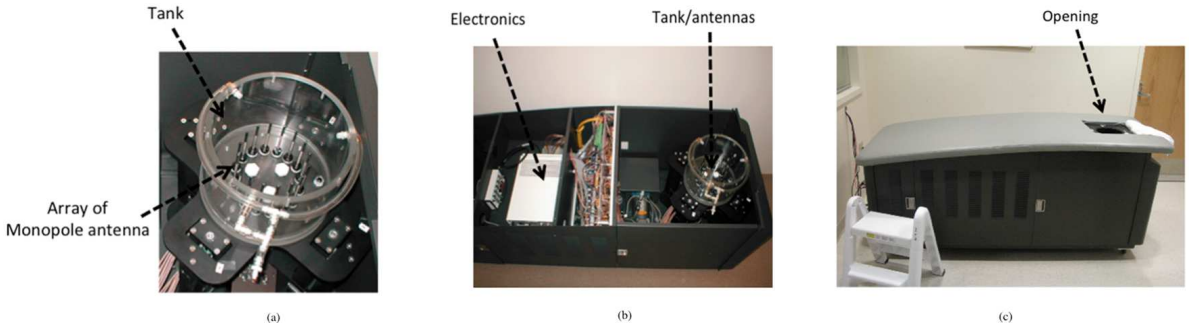

(a) Tank with antenna array. The tank is usually filled with a coupling liquid. The antennas are fully immersed in the liquid bath.

(b) Inside the examination table for MWI breast cancer detection: tank, antenna array, and microwave components.

(c) Examination table for MWI breast cancer detection at Dartmouth-Hitchcock Medical Center.

Fig. 1. MWT system at Dartmouth Hitchcook Medical Center.

$$\nabla \cdot (\underline{\underline{\mu}} \cdot \mathbf{H}) = 0 \tag{4}$$

where $\underline{\underline{\epsilon}}$ and $\underline{\underline{\mu}}$ are the diagonal permittivity and permeability tensors with $\underline{\underline{\epsilon}} = \epsilon_0(\underline{\underline{\epsilon_r}} - j\frac{\underline{\underline{\sigma}}}{\omega\epsilon_0})$, and ϵ_0 the free space permittivity. By substituting (1) into (2), one can obtain the "curl-curl" formulation [12] for the electric field, which is the tensorial wave equation:

$$\nabla \times [\underline{\underline{\mu}}^{-1} \cdot (\nabla \times \mathbf{E})] - k_0^2 \underline{\underline{\epsilon}} \cdot \mathbf{E} = 0 \tag{5}$$

In solving (1)-(4) different choices regarding the basis functions are available. Commonly, two kind of basis functions are used: nodal or edge basis functions. The use of nodal basis functions has been proposed for solving three-dimensional vector field problems [6]. The derivatives of the basis functions are not continuous and, if employed, the finite element solutions can be nonphysical, as the divergences for both the magnetic and electric field are not fulfilled (eqns. (3), and (4)). To overcome this problem, Paulsen and Lynch [13] explicitly enforced the divergence condition while scalar basis functions were used. Therefore, to completely avoid spurious solutions, a continuous derivative basis function is needed. More recently, it is well understood that edge basis function (zero order Whitney form, [5]), can solve the spurious modes problem for time-harmonic electromagnetics. It should be also noted that problems might occur for the electrostatic case (low-frequency breakdown) but alternative formulations based on potentials [14], for instance, can alleviate this numerical issue.

With regards to (5), we choose the edge basis functions, $\mathbf{W}$, and apply the Galerkin testing procedure in order to produce a discretized version of the functional:

$$\begin{aligned} M_{pq} = \iiint_V (\nabla \times \mathbf{W}_p) \cdot [\underline{\underline{\mu}}]^{-1} \cdot (\nabla \times \mathbf{W}_q) dV + \\ -k_0^2 \iiint_V \mathbf{W}_p \cdot [\underline{\underline{\epsilon_r}}] \cdot \mathbf{W}_q dV + \\ +j\omega\mu_0 \iiint_V \mathbf{W}_p \cdot [\underline{\underline{\sigma}}] \cdot \mathbf{W}_q dV \end{aligned} \tag{6}$$

and

$$\overline{\overline{M}} \cdot \overline{e} = \overline{\alpha} \tag{7}$$

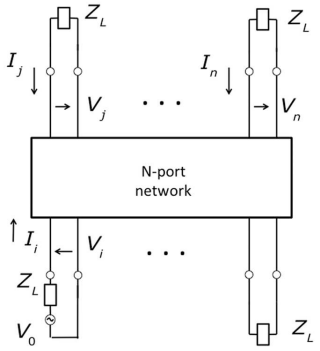

Fig. 4. Schematic representation for a N-port network. The MWT system has one transmitter and some receivers working at the same time. The transmitter port is excited with a voltage V_0 while the other are closed on Z_L.

where M_{pq} is the (p,q)th entry of the FEM matrix ($\overline{\overline{M}}$), $\underline{\underline{\epsilon_r}}$, $\underline{\underline{\sigma}}$ the relative permittivity and conductivity tensors respectively, $\overline{e}$ the solution coefficients, and $\overline{\alpha}$ in (7) the right-hand side (RHS) which will be discussed in Section III-B2. The reader is referred to [12] for the explicit expression of the basis function $\mathbf{W}$. The above discretized system (7) can therefore be used to describe the propagation of electromagnetic fields inside the MWT tank. Appropriate boundary conditions are applied for describing the presence of antennas, the excitations V_i and sensed voltages V_j at different ports, and the boundary of the tank.

B. Antennas and Coaxial Ports Modeling

The MWT system utilizes 16 antennas, which interface with the electronics through 3.5 mm SMA coaxial connectors. Over the range of frequencies at which the system is operated these connectors are unimodal, and operate in the Transverse ElectroMagnetic (TEM) mode. Excitations and sensed voltages V_i and V_j represent, therefore, TEM modal voltages at the antenna ports, and constitute the inputs and outputs of the system. Considering the schematic diagram in Fig. 4, the system can be modeled as a network with N ports at which excitations can be applied or voltages sensed. In practice appropriate boundary conditions are used in conjunction with (6) to describe:

- the presence of the metallic antennas in the volume of the tank;
- the applied excitations;
- sensed voltages computed from the FEM solution of (7).

These boundary conditions are discussed in the next three subsections.

1) Modeling Antennas: The MWT system uses monopole antennas obtained by stripping out the last 3.4 cm of the external shielding conductor of a rigid coaxial cable as illustrated in Fig. 2. This exposes the dielectric and the core conductor of the cable, and creates an *active part*. The coaxial shield and core, both metallic, are modeled as Perfectly Electric Conductors (PEC) by enforcing a Dirichlet boundary condition $\hat{n} \times \mathbf{E} = 0$ on all the mesh edges belonging to the surface of these two components. The dielectric insulator of the coaxial cable, which is exposed to the tank volume in the active part (Fig.5(b), and Fig. 5(c)), is simply modeled as a sub-volume with a known relative permittivity $\epsilon_r = 2.2$ and conductivity $\sigma = 0$ S/m; these values are representative for Teflon.

Of particular importance in describing the coupling between the antennas and the tank medium is the surface represented by the cross section of the antennas (Γ_{port}) at the level where the shield had been removed (Fig. 5(c)). Points below this surface are inside the cavity of the coaxial shield supporting the TEM mode while points above this surface are in the open field of the tank. The Γ_{port} surface is therefore the interface between the modal TEM propagation and the free propagation in the tank volume. In the following two next subsections we discuss how boundary conditions are used for describing the excitations and sensing voltages.

2) Modeling Port Excitations: Voltage excitations at Γ_{port} of any antenna is described using Dirichlet boundary conditions, and forcing the electric field distribution at that surface to be equal to the TEM modal distribution. Voltage excitation in the coax is enforced as a boundary condition for the electric field via the modal distribution:

$$\mathbf{E}_{\Gamma}^{(i)} = V_i \mathbf{e}^{\dagger} \tag{8}$$

where V_i the voltage between the inner and outer conductor of the *i*th coaxial cable, as applied by the driving electronics, $\mathbf{e}^{\dagger}$ is the TEM modal eigenfuction, and $E_{\Gamma}^{(i)}$ is the forced field at port $\Gamma^{(i)}$ of the *i*th antenna. The eigenfuction $\mathbf{e}^{\dagger}$ can be expressed as [15]:

$$\mathbf{e}^{\dagger} = \widehat{\rho} \frac{1}{\sqrt{2\pi \cdot ln(b/a)}} \frac{1}{\rho} \tag{9}$$

where a and b are the inner and outer diameters of the coaxial cable, and ρ is the local radial coordinate.

A RHS vector $\overline{\alpha}$ for the linear system (7) representing the above Dirichlet conditions can be found by testing the boundary condition on each Γ_{port} surface. The electric field can be expanded in terms of basis functions $\mathbf{W}$ as:

$$\mathbf{E} = \sum_{m \in \mathcal{M}} \alpha_m \mathbf{W}_m \tag{10}$$

where $\mathcal{M}$ is the set of edge indexes residing on Γ_{port}. Next, Galerkin testing is applied to the excitation boundary condition (8), yielding:

$$\sum_{m \in \mathcal{M}} \iint_{\Gamma_{port}} \mathbf{W}_m \cdot \mathbf{E} d\Gamma = \sum_{m \in \mathcal{M}} \sum_{n \in \mathcal{M}} \iint_{\Gamma_{port}} \alpha_m \mathbf{W}_m \cdot \mathbf{W}_n d\Gamma \tag{11}$$

The above is a linear system of equations, which can be expressed more explicitly:

$$\sum_{m \in \mathcal{M}} \sum_{n \in \mathcal{M}} \alpha_m \langle \mathbf{W}_m, \mathbf{W}_n \rangle = \langle \mathbf{W}_m, \mathbf{E}_{\Gamma}^{(i)} \rangle \tag{12}$$

The solution of the above system of equations allows computing the RHS $\overline{\alpha}$ representing the voltage excitations V_i at each *i*th port, and is used to model the applied excitations.

3) Modeling Sensed Voltages at Antenna Ports: In the MWT system all receiving antennas are closed on the matched impedance of the sensing electronics, and the sensed voltages are collected sequentially. As anticipated, the relation between currents and voltages of the N-port network which represents the system can be expressed using the Y-matrix [16]:

$$\overline{I} = \overline{\overline{Y}} \cdot \overline{V} \tag{13}$$

Additionally, a second condition is used for describing the source excitations and loading conditions:

$$\overline{V} = -\overline{\overline{Z}}_L \cdot \overline{I} + \overline{V}_{s_i} \tag{14}$$

where $\overline{\overline{Z}}_L = diag\{Z_L\}_L$ a $N \times N$ diagonal matrix with entries equal to the load Z_L, and $\overline{V}_{s_i}$ vector is expressed as follow:

$$\overline{V}_{s_i} = \begin{bmatrix} 0 \\ V_i \\ \vdots \\ 0 \end{bmatrix} \tag{15}$$

where the ith antenna is used as transmitter, and with $V_i = V_0$ (Fig. 4) the applied voltage eventually scaled to a desired power level. Substituting (14) into (13) and solving the system (13) for $\overline{V}$ it is possible to express the voltage at each port given the system excitation and loading conditions as:

$$\overline{V} = \overline{\overline{Y}}^{-1} \cdot (\mathbb{I} + \overline{\overline{Y}} \cdot \overline{\overline{Z}}_L)^{-1} \cdot \overline{\overline{Y}} \cdot \overline{V}_{s_i} \tag{16}$$

Knowledge of the Y-matrix facilitates computation of the received voltage at any port. In our approach we derive the Y-matrix of the system first, except for excitations and loading conditions, and then compute all the required voltages described above. The general entry of the admittance matrix is typically written as:

$$Y_{pq} = \frac{I_p}{V_q}\Big|_{V_k=0 \quad k \neq q} \tag{17}$$

where voltages, (18), and currents, (19), are defined as follows:

$$V_q = \frac{\iint_{\Gamma_{port}^{(q)}} \mathbf{E}^{(q)} \cdot \mathbf{e}^{\dagger}}{\iint_{\Gamma_{port}^{(q)}} \mathbf{e}^{\dagger} \cdot \mathbf{e}^{\dagger}} \tag{18}$$

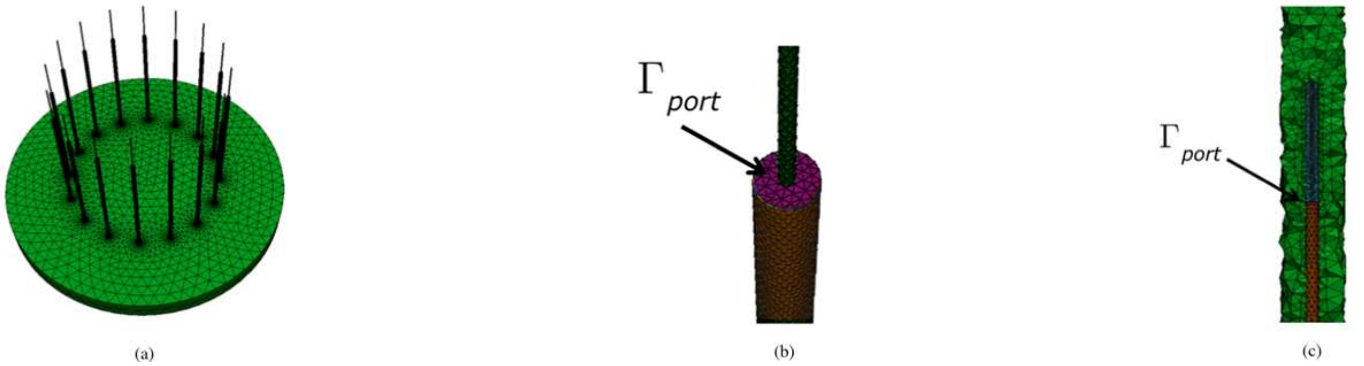

(a) FEM mesh showing the bottom plate of the imaging tank and the antennas. The interior of the tank, normally filled with a coupling liquid, and the side walls are not represented in this illustration, and in order to show the antennas we mesh only the internal conductor (metallic core).

(b) Expanded view for one monopole antenna: Γ_{port} is the surface between the coaxial cable and the active part (with the normal direction along the axis of the coax).

(c) Representation of the monopole antenna: the arrow indicates the $\Gamma port$ which is used to enforce/sense the field at the monopole antenna.

Fig. 5. Monopole antenna: antenna array mesh, and zoom-in for a single transmitter in order to show the Γ_{port} surface. The mesh for the external (dielectric) conductor is not shown in Fig.5(a), and 5(b) to better highlight the enforcing/sensing surface.

and

$$I_p = \frac{\iint_{\Gamma^{(p)}_{port}} \mathbf{H}^{(q)} \cdot \mathbf{h}^{\dagger}}{\iint_{\Gamma^{(p)}_{port}} \mathbf{h}^{\dagger} \cdot \mathbf{h}^{\dagger}} \tag{19}$$

being $\mathbf{E}^{(q)}$ and $\mathbf{H}^{(q)}$ the electric and magnetic field at the port when the qth transmitter is used, and ($\mathbf{e}^{\dagger}$ and $\mathbf{h}^{\dagger}$) are the electric and magnetic TEM modal eigenfunctions [15].

In essence the definition of the generic element of the Y-matrix, (17), indicates that this term can be obtained by applying an excitation V_q at the qth port, and by collecting the voltage V_p when all ports, with the exception of the qth port, are closed on a short circuit. The current term I_p involves the magnetic field, which can be computed by differentiating a forward solution as we solve for the electric field:

$$\mathbf{E}(\mathbf{r}) = \sum_{l=1}^{L} e_l \mathbf{W}_l(\mathbf{r}) \tag{20}$$

where $\{e\}_{l=1}^{L}$ are the solution coefficients. Consequently, the magnetic field can be obtained as follow:

$$\mathbf{H}(\mathbf{r}) = -\frac{1}{j\omega}[\underline{\underline{\mu}}]^{-1} \sum_{l=1}^{L} e_l \nabla \times \mathbf{W}_l(\mathbf{r}) \tag{21}$$

Knowledge of V_q and I_p allows for the computation of the element Y_{pq} of the Y-matrix. In general N forward solutions with unit excitations at each antenna are required to build the full Y-matrix and solve for the received voltages under specified excitation and loading conditions using (16).

4) Absorbing Boundary Conditions: In the MWT system, fields used for imaging, emitted by the antennas, are largely attenuated before reaching the walls of the tank by the presence of the lossy water/glycerin bath. From a numerical point of view, these fields could reflect off the walls of the tank, to generate spurious reflections. In order to ensure that unwanted reflections are suppressed Absorbing Boundary Conditions (ABC) are implemented. A suitable ABC condition that offers high absorption over a wide range of frequencies and for a generic incident angle is the perfectly matched layer (PML) introduced by Berenger [17]. The PML conditions are implemented using a layer of material with *ad-hoc* electrical properties that surrounds the imaging domain, illustrated in Fig. 3 as region $\Omega_{PML} = \cup_{i=1}^{3}\Omega_i$. The goal in using PML layers is to:

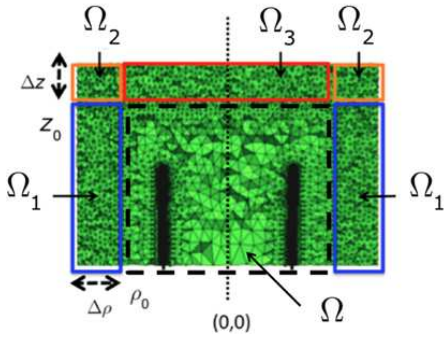

Fig. 6. Cross section of the FEM model of the tank, showing the PML regions. Three regions (Ω_1, Ω_2, Ω_3) are selected to match the tank boundaries and to attenuate the propagating waves.

- match the impedance at the interface between the layer and the domain (interface between region Ω_{PML} and Ω in Fig. 3), so that the fields enter the PML region without reflections.
- attenuate fields that travel thought the PML region, maintaining a matched impedance condition, so that fields eventually die out before reaching the boundary of the numerical domain.

The properties of PML materials can be designed to completely attenuate a wave incident on the PML layer along a set direction. Waves incident from other directions are attenuated by a factor that depends on the incidence angle: the closer this angle is to the optimal, the higher is the attenuation. Given that the PML has a preferential direction of attenuation, it is common to use a number of layers to cover the boundary of the domain, each optimized for the average direction of the waves incident on that portion of boundary. In our case we use three different layers: 1) a first layer is used on the side walls of the domain (indicated as Ω_1 in Fig. 6), this layer is designed to offer maximum attenuation for waves propagating radially; 2) a second layer is used for the top of the tank (indicated as Ω_3 in Fig. 6), and is designed to offer maximum attenuation for waves traveling vertically; 3) a third layer is used at the corner between the side and top walls of the tank (indicated as Ω_2 in Fig. 6), and is designed to offer maximum attenuation for waves that hit this layer at a 45 degrees angle.

To express the PML properties for waves propagating radially, it is convenient to use cylindrical coordinates. Equations (1) - (4) are obtained by using the nabla operator [18] (for cylindrical coordinates) and rewriting as:

$$\tilde{\nabla} = \hat{\rho}\frac{1}{s_\rho}\frac{\partial}{\partial\widetilde{\rho}} + \hat{\phi}\frac{1}{\widetilde{\rho}}\frac{\partial}{\partial\phi} + \hat{z}\frac{1}{s_z}\frac{\partial}{\partial z} \tag{22}$$

where s_ρ, $\widetilde{\rho}$, and s_z are frequency independent terms called *complex stretching variables* [19], [20]. When $s_\rho = s_z = 1$, and $\widetilde{\rho} = \rho$ the fields computed with the nabla operator in (22) are the traditional Maxwell's equations in cylindrical coordinates. Following results in [21], the stretching variables for the imaging domain Ω and the three PML regions $\Omega_{1,2,3}$ can be set as follows:

$$\begin{cases} s_\rho(\rho) = 1 \\ \widetilde{\rho}(\rho) = \rho \\ s_z(z) = 1 \end{cases} \qquad \rho,\, z \in \Omega \tag{23}$$

$$\begin{cases} s_\rho(\rho) = 1 - j\alpha\left(\frac{\rho-\rho_0}{\Delta\rho}\right)^2 \\ \widetilde{\rho}(\rho) = \rho - j\alpha\frac{(\rho-\rho_0)^3}{3\Delta\rho^2} \\ s_z(z) = 1 \end{cases} \qquad \rho,\, z \in \Omega_1 \tag{24}$$

$$\begin{cases} s_\rho(\rho) = 1 - j\alpha\left(\frac{\rho-\rho_0}{\Delta\rho}\right)^2 \\ \widetilde{\rho}(\rho) = \rho - j\alpha\frac{(\rho-\rho_0)^3}{3\Delta\rho^2} \\ s_z(z) = 1 - j\beta\left(\frac{z-z_0}{\Delta z}\right) \end{cases} \qquad \rho,\, z \in \Omega_2 \tag{25}$$

$$\begin{cases} s_\rho(\rho) = 1 \\ \widetilde{\rho}(\rho) = 1 \\ s_z(z) = 1 - j\beta\left(\frac{z-z_0}{\Delta z}\right)^2 \end{cases} \qquad \rho,\, z \in \Omega_3 \tag{26}$$

where α and β two real-valued parameters that take into account the contrast at the interface between Ω and Ω_{PML}, and the attenuation of the waves propagating through Ω_{PML}. In this manuscript we have chosen $\alpha = \beta = 6$ as suggested by [22]. The above stretching variables guarantee the desired attenuation of the fields incident on the PML layers, and can be translated in the dielectric properties of the generic medium in regions Ω, Ω_1, Ω_2, Ω_3 by using the following tensors:

$$\underline{\underline{\epsilon}} = \epsilon\underline{\underline{\Lambda}} \qquad \underline{\underline{\mu}} = \mu\underline{\underline{\Lambda}} \tag{27}$$

where $\epsilon = \epsilon_0(\epsilon_r - j\frac{\sigma}{w\epsilon_0})$, $\mu = \mu_0\mu_r$, and $\underline{\underline{\Lambda}}$ is expressed as:

$$\underline{\underline{\Lambda}} = \widehat{\rho}\widehat{\rho}\left(\frac{\widetilde{\rho}}{\rho}\right)\left(\frac{s_z}{s_\rho}\right) + \widehat{\phi}\widehat{\phi}\left(\frac{\rho}{\widetilde{\rho}}\right)(s_z s_\rho) + \widehat{z}\widehat{z}\left(\frac{\widetilde{\rho}}{\rho}\right)\left(\frac{s_\rho}{s_z}\right) \tag{28}$$

Translating the PML conditions in matrical properties allows handling these conditions without substantial modifications to the base FEM implementation. Each tetrahedral element in a PML region for local tensor $\underline{\underline{\Lambda}}$, depending on the location of the element, is computed. As the FEM system (7) is expressed in Cartesian coordinates, the tensor is expressed in this system using a transformation matrix defined as follow:

$$\underline{\underline{J}} = \begin{bmatrix} cos(\theta) & -sin(\theta) & 0 \\ sin(\theta) & cos(\theta) & 0 \\ 0 & 0 & 1 \end{bmatrix} \tag{29}$$

where θ is the azimuthal angle computed with respect to the mid-point of the tetrahedral mesh element. The tensor in Cartesian coordinates is then obtained as $\underline{\underline{\Lambda}}_{[x,y,z]} = \underline{\underline{J}}^T \cdot \underline{\underline{\Lambda}} \cdot \underline{\underline{J}}$. The material properties of the tetrahedral element can be expressed as:

$$\underline{\underline{\epsilon}} = \epsilon\underline{\underline{\Lambda}}_{[x,y,z]} \qquad \underline{\underline{\mu}} = \mu\underline{\underline{\Lambda}}_{[x,y,z]} \tag{30}$$

Finally, we close the exterior surface of the numerical domain with a PEC condition ($\hat{n} \times \mathbf{E} = 0$). As the propagating fields are attenuated by the PML, this condition results in no reflections.

IV. Results

The edge-based FEM proposed in the preceding sections was used to develop a model for the Dartmouth MWT system [4]. In the present section we report firstly results from numerical simulations which have been used as a preliminary validation of the model. Secondly the model is compared against a set of experimental results, showing a good matching between model predicted measurements and actual measurements.

As mentioned in Section II, in the normal operation of the MWT system the tank is filled with a coupling liquid in order to reduced unwanted reflections at the air/skin interface with the breast. A possible choice for such a liquid is a mixture of glycerin and water. In order to reproduce the same working conditions we used a 80:20 glycerin-water bath to fill the tank and completely submerge the antennas (Fig. 7 shows the dielectric properties of two liquids). All the receiving antennas are terminated with a resistive load of $Z_L = 50\Omega$ (Fig. 4), and here we also note that the antennas must be fully immersed to work properly.

The MWT system is is modelled with a 3-D FEM tetrahedral mesh produced with Netgen mesh generator [23], [24]. For all results here reported we employ a Dell Optiplex PC, Windows 7, 64-bit, with Intel i7-2600 CPU at 3.40 GHz, and 16 GB of memory. With regards to the solution of the

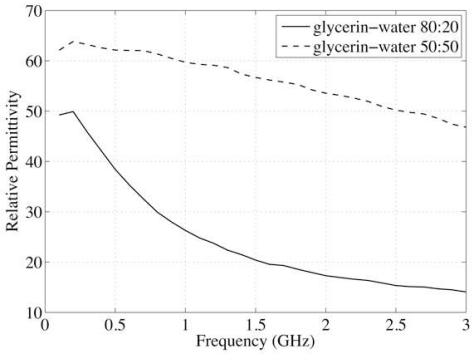

(a) Relative permittivity for liquids used as bath and scatterer.

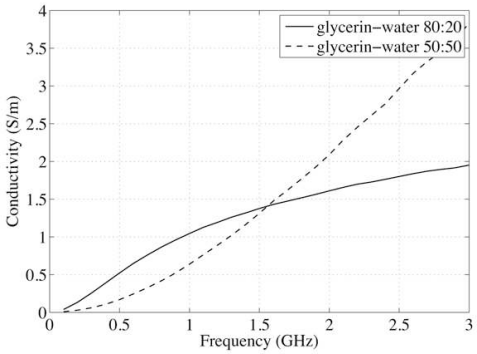

(b) Conductivity (S/m) for liquids used as bath and scatterer.

Fig. 7. Dielectric properties for 80:20 and 50:50 glycerin-water from 100 MHz up to 3000 MHz. The 50:50 glycerin-water mixture is used to simulate a scatterer due to the differences (contrast) in the considered dielectric properties, while we use the 80:20 mixture as coupling liquid.

discretized system of matrix equations, we use a multi-frontal PARDISO solver [25].

Along with the numerical simulations (Section IV-A), we conducted two experiments at 900 and 1900 MHz. In the first experiment, Section IV-B, we consider only the tank with the coupling liquid at 900 MHz. Then, we place a scatterer and we run two experiments: Section IV-C at 900 MHz, and Section IV-D at 1900 MHz.

A. Numerical experiment

In this section we report results from numerical simulations by analyzing the fields radiated from one transmitter of the physical MWT system. We applied the formulation proposed in Section III-A jointly with the novel procedures presented in Section III-B2 to enforce a modal voltage distribution.

In this numerical test, we simulate a working scenario with a scatterer placed inside the imaging domain. We chose a 3 cm diameter plexiglass cylinder extending the full height of the tank. Figure 11(a) depicts a schematic representation of the experiment, and 11(b) shows a top-view of the tank with the dielectric cylinder inside. To mimic the presence of a scatterer inside the tank we used a plexiglass cylinder placed as in Fig.11(a), and with a 50:50 glycerin-water mixture. Using a different concentration of this liquid allows us to represent a scatterer with different electrical properties as depicted in Fig.7. At f=1900 MHz the dielectric properties of the liquid bath are $\epsilon_{r_{bk}} = 18.22$, $\sigma_{bk} = 1.66$ S/m while those for the scatterer are $\epsilon_{r_{sc}} = 54.23$, $\sigma_{sc} = 1.92$ S/m. In the following we consider $N_{TX} = 16$ antennas. For the ith transmitter a unique set of $N_{RX} = N_{TX} - 1$ receivers is available. Thus, for N_{TX} transmitters we collect $M = N_{TX} \times (N_{TX} - 1)$ data, $M = 240$ samples. We note that the measurement quantity is the voltage associated with each antenna, and that the simulated amplitude of the received voltages for the closest transmit-receive configurations have been eliminated due to saturation of the receivers.

The tank with all the antennas, and the scatterer placed inside are discretized with edge-based FEM yielding 2,563,313 tetrahedra (3,145,794 unknowns). With regard to the sparse FEM matrix assembling phase, we code some C/C++ functions; these functions have been optimized taking into account assembling time and memory occupancy.

The solution time for the discretized system of matrix equation (7) (using PARDISO) is roughly 4 hours for all $N_{TX} = 16$ transmitters. The reader should notice that this may not the most efficient solver for such a kind of problem. Using an iterative method with an appropriate preconditioner technique might result in a faster solution. For this complex Helmholtz problem, the Domain Decomposition Method (DDM) seems to be a suitable candidate for solving large system matrices arising from FEM discretization [26]–[28]. We note that the development of a DDM preconditioner is currently under way, and that preliminary results can be found in [29].

Fig. 8 shows normalized z-component of the electric field magnitude and phase. First, the information carried by the phase is crucial because by visual examination, it is possible to infer the position of the scatterer. Next, we tested the employed PML: for proper operation, phase continuity must be preserved across the PML-layer [17]. From Fig. 8(b) it is clear that the emitted wave is propagating from the transmitter through the discretized tank without reflections.

It was demonstrated in [11] that the monopole radiation in a lossy bath exhibits a pattern very close to spherical-like radiation. Given that the antenna lacks a symmetrizer (balun), one would expect a significant current on the outer surface of the feeding coaxial line (*Sommerfeld-Goubau wave* [30]). However, due to large damping of the lossy medium the radiated field actually remains nearly spherical with the phase center located approximately at the middle of the active part of the monopole. In order to closely verify this conjecture, we employed our numerical solution; the most relevant assessment is carried out through analyzing the real part of the Poynting vector $\mathbf{S}$:

$$\mathbf{S} = \frac{1}{2}\mathbf{E} \times \mathbf{H}^* \tag{31}$$

Fig. 9 shows the normalized real part of the Poynting vector $\mathbf{S}$ at f=1900 MHz in a cross section including the transmitter and the opposite receiver. It can be seen that while the perturbation of the unbalancing is evident close to the coaxial-monopole

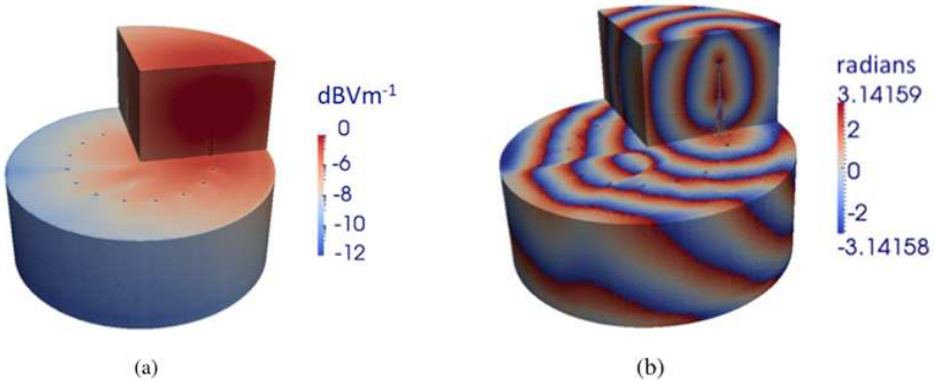

(a) (b)

(a) Magnitude of E_z component on multiple slices.

(b) Phase for Ez component. The position of the scatterer is clearly observed due to the phase distortion.

Fig. 8. Simulation experiment: electric field (Ez).

transition, the disturbance diminishes away quickly from the Γ_{port}.

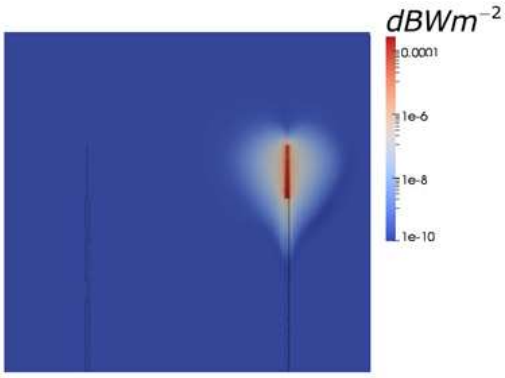

Fig. 9. Normalized real part of Poynting vector $\mathbf{S}$ at f=1900 MHz showing the energy deposition of the selected monopole antenna.

B. Experiment 1

In the MWT system, the array of antennas is able to move up and down utilizing linear actuator motors yielding multiple in-plane and cross-plane data acquisitions. For this analysis we acquired data only from one plane at the distance of 4 cm from the top of the tank.

In this experiment we tested the ability of accurately reproduce the measurements in the absence of scatterers; the tank was filled with a uniform glycerin-water 80:20 percent solution (coupling liquid).

The complete MWT system was discretized at f=900 MHz with 1,807,965 tetrahedra and 2,234,380 unknowns; the solution time for the system of sparse linear equations resulting from FEM disctretization is roughly 1 hour. The relative permittivity and conductivity of the background bath at 900 MHz are $\epsilon_{r_{bk}} = 28.9$, and $\sigma_{bk} = 0.96$ S/m, respectively. Fig. 10 depicts the measured and simulated voltage for all transmitter/receiver pair, and shows strong agreement between simulations and measurements. We note that the magnitude of measured and simulated voltages for all transmitter/receiver pair agree better than 2.3648 dBm.

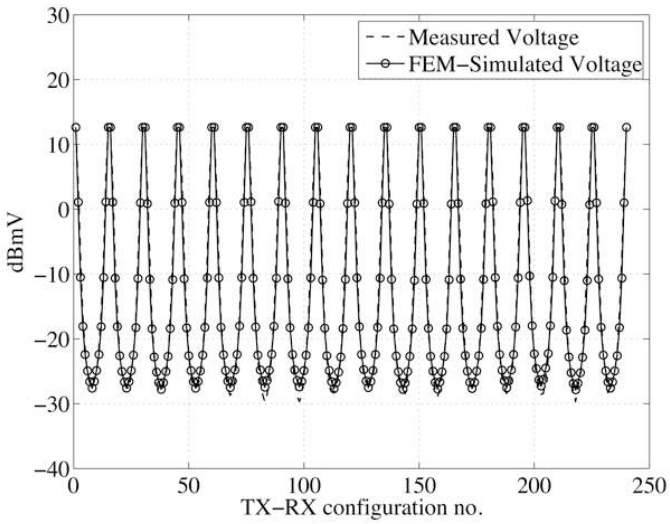

Fig. 10. Experiment 1: magnitude of measured and simulated voltage for 240 different excitations and sensing configurations resulting from rotating the excitation and the sensing antennas. At this level of magnification the simulated and measured fields completely superimpose, as they are matching closely. Other figures show magnified views, where it is possible to appreciate discrepancies between simulations and synthetic data.

C. Experiment 2

In this experiment we simulate the tank with an inclusion. Geometrical information about position and size of the scatterer can be found in Section IV-A. The dielectric properties of the liquid bath at 900 MHz are $\epsilon_{r_{bk}} = 28.9$, $\sigma_{bk} = 0.96$ S/m while those for the scatterer are $\epsilon_{r_{sc}} = 60.48$, $\sigma_{sc} = 0.52$ S/m. The discretized MWT system consists of 2,223,753 tetrahedra with 2,705,568 unknowns; the matrix system (7) was solved in 4140 sec.

Fig. 12 shows magnitude and phase for 6 transmitters and relative receiver antenna positions ($M = 90$). We see that the magnitude of measured and simulated voltages agree better than 1.9907 dBm, while the phase agrees better than 14°. To

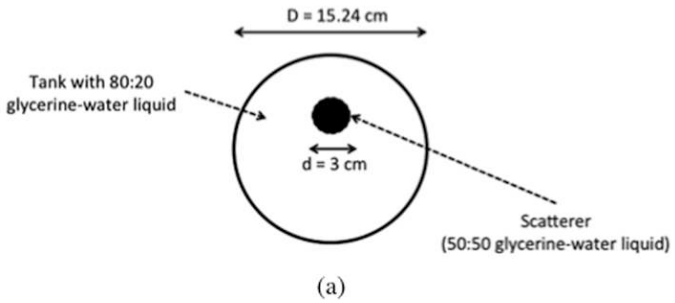

(a) A cylindrical scatterer is placed inside the tank at the position represented the dark circle.

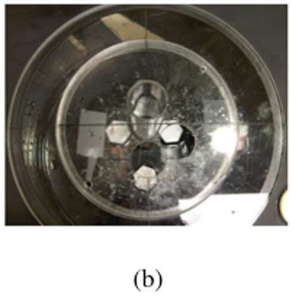

(b) Top view of tank with the scatterer.

Fig. 11. Experiment 2: representation of the setup and picture of the experiment.

quantify the accuracy of the simulations and compare them with the measurements, we consider the average error per data point defined as follow:

$$\text{Err} = \frac{\|\overline{V}^{meas} - \overline{V}^{sim}\|}{M} \tag{32}$$

Considering $M = 240$ (all TX/RX pairs), in this experiment Err is 1.36%; this demonstrates that we were able to predict the magnitude and phase measurements when a scatterer is placed inside the tank.

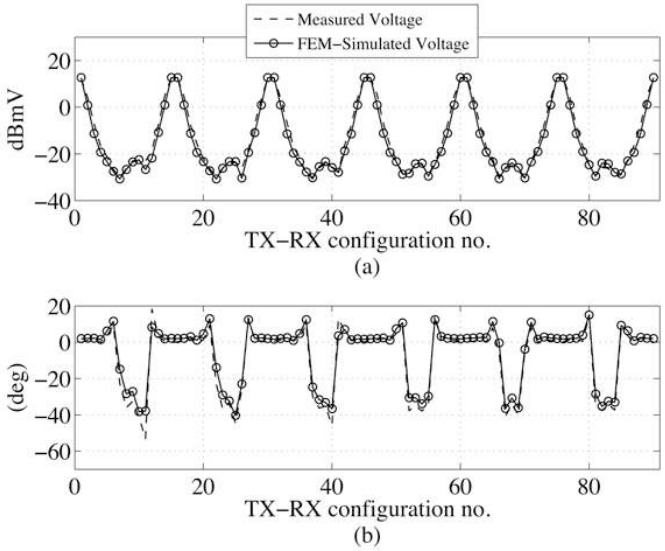

Fig. 12. Experiment 2: dielectric cylinder inside tank. TX-RX configurations for 6 transmitters resulting in $M = 90$ data points; a) magnitude and b) phase of measured and simulated received voltages. At this level of magnification the simulated and measured fields completely superimpose, as they are matching closely.

D. Experiment 3

With regard to the experiment presented in Section IV-A, we compared measured and simulated data in order to demonstrate that our model is able to predict the measurements even at a relatively high frequency, 1900 MHz. The dielectric properties of the liquid bath are $\epsilon_{r_{bk}} = 18.22$, $\sigma_{bk} = 1.66$ S/m while those for the scatterer are $\epsilon_{r_{sc}} = 54.23$, $\sigma_{sc} = 1.92$ S/m. The position and size of the inclusion are shown in Fig. 11(a). The discretization procedure produces 2,563,313 tetrahedra which corresponds to 3,145,794 unknowns. We show in Fig. 13 the comparison of measurements and simulations at f=1900 MHz.

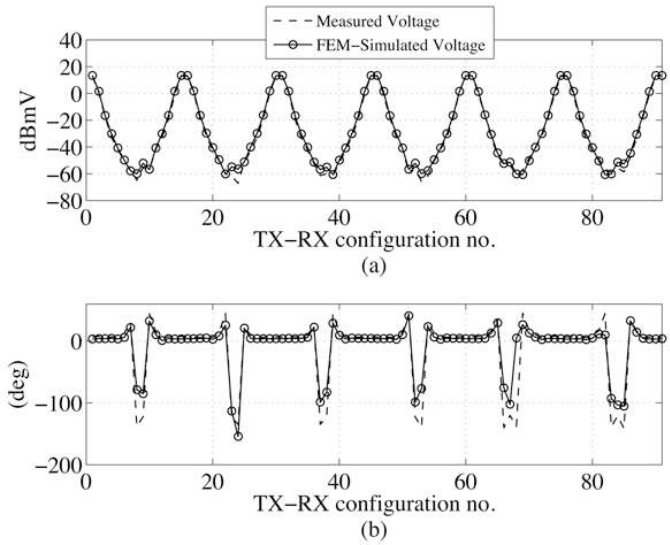

Fig. 13. Experiment 3: magnitude a) and phase b) of measured and simulated voltage for 6 transmitters (and relative receivers) at f=1900 MHz. At this level of magnification the simulated and measured fields completely superimpose, as they are matching closely.

To allow for a closer comparison, we select one of the employed 16 monopole antennas, and we show the magnitude and phase results separately for the relative receivers in Fig 14. According to Fig. 14 small discrepancies (6 dBm) occur for the magnitude voltage of the relative receiver number 7, and 8, while the phase error between measures and simulations is roughly 40°at the lower level of this extremely wide dynamic range. The average error per data point (Err) is 0.9% ($M = 240$ in (32)).

V. Conclusions

An accurate forward model is a necessary starting point for inverse scattering algorithms. In particular, the modeling should be able to accurately predict the quantities that are actually measured in a real-life system. To this end, we have proposed and validated a whole-system full-wave modeling method for microwave tomography based on the Edge Finite

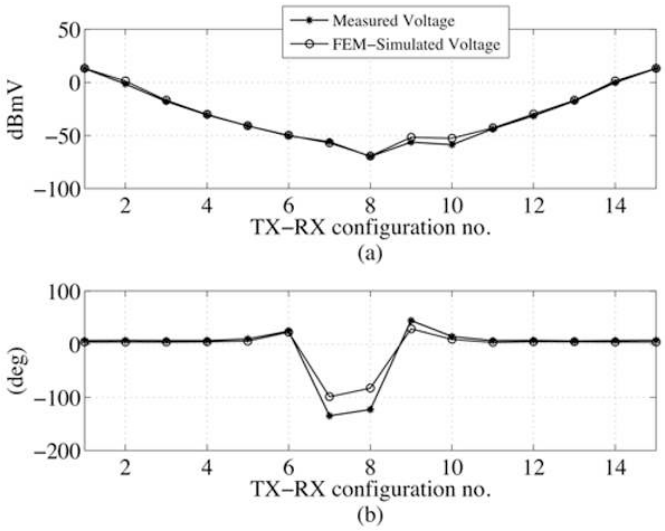

Fig. 14. Experiment 3: magnitude and phase for measured and simulated voltage for the selected transmitter. These graphs, representing magnitude and phase of the simulated and experimental measurements, have been expanded to show this data in grater detail. As it is possible to notice, a very close agreement is found between simulated and measured data.

Element Method. The approach considers the full material and geometric properties of the system, uses the actual excitation at antenna ports, and renders the measured received signals with specified loading terminations without approximations or simplifying assumptions. This is obtained by characterizing the generic microwave imaging system as an N-port structure via its admittance matrix, whose entries carry all the information on the content of the region of interest. This allows a straightforward inclusion of port excitation and terminations which is made possible by a specialized, rigorous field-based description of the port boundary conditions employing a modal representation of the field in the connecting coaxial lines. Experimental tests have been conducted showing good agreement between measured and simulated data, and the numerical tool has also proven useful in understanding the wave physics of tomographic equipment.

ACKNOWLEDGEMENT

The authors would like to thank Dr. F. P. Andriulli for the inspiring discussions on finite element method in electromagnetics.

REFERENCES

[1] M. Lazebnik, D. Popovic, L. McCartney, C. Watkins, M. Lindstrom, J. Harter, S. Sewall, T. Ogilvie, A. Magliocco, T. Breslin, W. Temple, D. Mew, J. Booske, M. Okoniewski, and S. Hagness, "A large- scale study of the ultrawideband microwave dielectric properties of normal, benign and malignant breast tissues obtained from cancer surgeries," *Physics in Medicine and Biology*, vol. 52, pp. 6093–6115, 2007.

[2] E. Bond, X. Li, S. C. Hagness, and B. V. Vee, "Microwave imaging via space-time beamforming for early detection of breast cancer," *IEEE Trans. Antennas Propag.*, vol. 51, pp. 1690–1705, August 2003.

[3] A. Tikhonov and V. Arsenin, *Solutions of ill-posed problems*. Wiley and Sons, 1977.

[4] K. Paulsen, P. Meaney, and L. Gilman, *Alternative Breast Imaging*. Springer-Verlang, 2005.

[5] J. Nedelec, "Mixed finite elements in r^3," *Numerische Mathematik*, vol. 28, no. 35, pp. 315–342.

[6] P. Sylvester and R. Ferrari, *Finite Element for Electrical Engineerings*. Cambridge University Press, 1996.

[7] W. C. Chew, Z. Nie, Q. Liu, and Y. Lo, "Analysis of probe-fed microstrip disk antenna," *IEE Proceedings-H*, vol. 138, April 1991.

[8] D. Milanesio, O. Meneghini, V. Lancellotti, R. Maggiora, and G. Vecchi, "A multi-cavity approach for enhanced efficiency in topica rf antenna code," *Nuclear Fusion*, vol. 46, pp. 476–499, 2009.

[9] E. A. Attardo, A. Borsic, P. M. Meaney, and G. Vecchi, "Finite element modeling for microwave tomography," in *Antennas and Propagation (APS-URSI)*, IEEE International Symposium, pp. 703–706, July 2011.

[10] M. Haynes, J. Stang, and M. Moghaddam, "Microwave breast imaging system prototype with integrated numerical characterization," *International Journal of Biomedical Imaging*, 2012.

[11] C. J. Fox, P. M. Meaney, F. Shubitidze, L. Potwin, and K. D. Paulsen, "Characterization of an implicitly resistively-loaded monopole antenna in lossy liquid media," *Int. J. of Ant. and Prop.*, vol. 28, 2008.

[12] J. Jin, *The Finite Element Method in Electromagnetics*. Wiley and Sons, second edition ed., 2002.

[13] K. D. Paulsen and D. Lynch, "Elimination of vector parasites in finite element maxwell solutions," *TMTT*, vol. MTT39, pp. 395–404, 1991.

[14] R.Dyczlj-Edllnger, G. Peng, and J.-F. Lee, "Efficient finite element solvers for the maxwell equations in the frequency domain," *Comput. Methods Appl. Mech. Eng.*, vol. 169, pp. 297–309, 1999.

[15] N. Marcuvitz, *Waveguide Handbook*. New York: McGraw-Hill, 1951.

[16] D. Pozar, *Microwave Engineering*. Wiley and Sons, 4th ed., 2011.

[17] J. Berenger, *Perfectly Matched Layer for Computational Electromagnetics*. Morgan and Claypool, 1994.

[18] W. C. Chew, J. Jin, E. Michielssen, and J. Song, *Fast and Efficient algorithms in computational electromagnetics*. Artech house, 2001.

[19] W. C. Chew, "A 3d perfectly matched medium from modified maxwell's equation with stretched coordinate," *Micr. Opt. Tech. Let.*, 1994.

[20] J. Maloney, M. Kesler, and G. Smith, "Generalization of pml to cylindrical geometries," *13th Annu. Rev. Progress Appl. Computa. Electromagn.*, vol. II, 1997.

[21] A. Greenwood and J. Jin, "A novel efficient algorithm for scattering from a complex bor using mixed finite elements and cylindrical pml," *IEEE Trans. Antennas Propag.*, vol. 47, pp. 620–629, April 1999.

[22] J. Fang and Z. Wu, "Generalized perfectly matched layer for the absorption of propagation and evanescent waves in lossless and lossy media," *IRE Trans. Microw. Theory Tech.*, vol. 44, no. 12, pp. 2216–2223, 1997.

[23] "http://www.hpfem.jku.at/netgen/."

[24] J. Schoberl, "Netgen - an advancing front 2d/3d-mesh generator based on abstract rules," *Computing and Visualization in Science*, vol. 1, pp. 41–52, 1997.

[25] "http://www.pardiso-project.org/."

[26] M. N. Vouvakis, Z. Cendes, and J.-F. Lee, "A fem domain decomposition method for photonic and electromagnetic band gap structures," *IEEE Trans. Antennas Propag.*, vol. 54, no. 2, pp. 721–733, Feb. 2006.

[27] K. Zhao, V. Rawat, S.-C. Lee, and J.-F. Lee, "A domain decomposition method with noncorfomal meshes for finite periodic and semi-periodic structures," *IEEE Trans. Antennas Propag.*, vol. 55, pp. 2559–2570, September 2007.

[28] Y.-L. Li and J. Jin, "A new dual-primal domain decomposition approach for finite element simulation of 3-d large-scale electromagnetic problems," *IEEE Trans. Antennas Propag.*, vol. 55, pp. 2803–2810, October 2007.

[29] E. A. Attardo and G. Vecchi, "Microwave tomography via domain decomposition for finite element methods," in *IEEE AP-S URSI Symp., Chicago, IL, USA (accepted)*, July 2012.

[30] R. Collin, *Field Theory of Guided Waves*. Wiley-IEEE Press, 1990.